Modeling of Io-Jupiter Decameter Arcs, Emission Beaming and Energy Source

Sébastien L. G. Hess, Baptiste Cecconi, Philippe Zarka

Modeling of Io-Jupiter decameter arcs, emission beaming and energy source

S. Hess,[1,2] B. Cecconi,[1] and P. Zarka[1]

Received 15 February 2008; revised 29 May 2008; accepted 11 June 2008; published 12 July 2008.

[1] The electrodynamic interaction between Io and Jupiter causes electron acceleration in/near the Io flux tube (IFT), which in turn produces intense radio emissions in the hecto-decameter range, displaying arc shapes in the time-frequency plane. The shapes depend on the hemisphere of origin of the emission and on the Io-Jupiter-observer geometry. Assuming radio wave generation by the cyclotron-maser instability, we simulate t-f arc shapes as a function of emission beaming, lead angle between the radio emitting field line and the instantaneous Io field line, and electron energy. A good fit of arcs t-f location and shape is obtained for loss-cone driven (oblique) emission beamed in a hollow cone of half-angle $\geq 80°$ around the source magnetic field, closing at high frequencies, and of cone thickness $\leq 1°$. The lead angle is found between a few degrees and $\sim 40°$ in both hemispheres. Resonant electron energies are about a few keV. Implications on the absence of a plasma cavity at IFT footprints and on Jupiter's internal magnetic field model are discussed. **Citation:** Hess, S., B. Cecconi, and P. Zarka (2008), Modeling of Io-Jupiter decameter arcs, emission beaming and energy source, *Geophys. Res. Lett.*, *35*, L13107, doi:10.1029/2008GL033656.

1. Introduction

[2] The electrodynamic interaction between Io and Jupiter is known to lead to accelerated electrons in/near the Io flux tube (IFT) [*Saur et al.*, 2004, and references therein]. These electrons produce intense radio emissions in between ~ 1 and 40 MHz, with specific arc shapes in the time-frequency (t-f) plane, as well as ultraviolet (UV) and infrared (IR) spots at/near the IFT ionospheric footprints [*Prangé et al.*, 1996].

[3] The perturbation caused by Io in Jupiter's magnetic field takes several minutes to propagate along the IFT from Io to Jupiter (probably at Alfvén speed) [*Neubauer*, 1980]. During this time, Jupiter's rotation, which is faster than Io's orbital motion, carries the perturbed field lines ahead of Io. The field lines along which electron acceleration and radio emission occur lead Io by an angle δ, which depends on the plasma and field characteristics around Io and thus on its Jovigraphic longitude Λ_{Io} and its north-south position within the torus. Radio emission characteristics are consistent with generation via the cyclotron maser instability (CMI), i.e., with emission frequency $f \sim f_{ce}$ (with f_{ce} the local electron cyclotron frequency).

[4] CMI causes maximum amplification of the radiation at large angles from the local magnetic field, so that the beaming pattern of a source, at a given frequency, is a hollow cone with a large aperture angle and an axis parallel to the magnetic field in the source. This anisotropic beaming causes four typical shapes of Io-Jupiter radio arcs to be observed in the t-f plane, related to the so-called Io$-$A, $-$B, $-$C and $-$D "sources" [*Carr et al.*, 1983]. These sources actually correspond to the vicinity of the northern (A & B) and southern (C & D) IFT footprints, seen from either side of the radio emission cone, i.e. when Io is at the eastern (A & C) or western (B & D) limb of Jupiter. Identical Io-Jupiter-observer geometries lead to identical radio arcs shapes observed.

[5] *Queinnec and Zarka* [1998] (hereinafter referred to as QZ98) performed a 3D geometrical analysis of a few arc shapes and deduced that they result from the combination of the magnetic field topology at the source, the CMI beaming pattern, and the source-observer geometry. The two key parameters are: (i) the radio beaming angle $\theta(f)$ between the source magnetic field and the direction of maximum emission at each frequency, and (ii) the lead angle $\delta(\Lambda_{Io})$ between the field line carrying the instantaneous radio source ("active" field line) and the instantaneous Io field line. Both parameters may differ at a given time for radio emissions from the northern and southern Jovian hemispheres. QZ98 found θ about $70°-80°$ at low frequencies, decreasing toward high frequencies, and δ between $10°$ and $40°$.

[6] Here we directly simulate Io-Jupiter arc shapes in the t-f plane by computing the geometrical visibility of radio sources located along an active field line, with the emission geometry being constrained by the physics of the CMI. The aim is twofold: (i) check if only the observed arcs are predicted by the model, and (ii) constrain in both hemispheres the cone aperture function $\theta(f)$, its thickness $\delta\theta$, the lead angle $\delta(\Lambda_{Io})$, the energy of resonant electrons, and the Jovian magnetic field model.

[7] The radio beaming angle $\theta(f)$ predicted by the CMI, as a function of the unstable electron distribution generating the radiation, is discussed in section 2. Our simulation method and software is presented in section 3, and the results are discussed in section 4. Perspectives are outlined in the last section.

2. Radio Emission and Beaming

[8] The CMI is thought to be responsible for all planetary high latitude radio emissions, including auroral and Io-Jupiter decameter emissions. It is a resonant interaction between electrons with a characteristic velocity v gyrating around magnetic field lines with a circular frequency ω_{ce}

[1]LESIA, Observatoire de Paris, UPMC, Université Paris Diderot, CNRS, Meudon, France.
[2]Also at LUTH, Observatoire de Paris, CNRS, Meudon, France.

0094-8276/08/2008GL033656

and a circularly polarized wave with frequency $\omega = 2\pi f$. The resonance condition is:

$$\omega = \omega_{ce}/\Gamma + k_{\|} v_{\|} \quad (1)$$

where Γ is the relativistic Lorentz factor, k the wave vector, v the electron velocity, and the subscript $_{||}$ refers to the direction of the local magnetic field in the source [*Wu*, 1985; *Pritchett et al.*, 2002]. This equation defines a circle in the velocity plane, centered on:

$$\begin{aligned} v_{\|o} &= \left(k_{\|} c^2/\omega_{ce}\right)\mathbf{b} = (\omega c N/\omega_{ce})\mathbf{k}.\mathbf{b}/k \\ &= (\omega c N/\omega_{ce})\cos\theta \sim c\cos\theta \end{aligned} \quad (2)$$

with $\omega \sim \omega_{ce}$ and N the refraction index given by the Appleton-Hartree dispersion relation in the cold plasma approximation. We assume here $N \sim 1$ since the Jovian radiosources are strongly magnetized, i.e., $\omega_{ce} \gg \omega_{pe}$ (with ω_{pe} the plasma frequency).

[9] The CMI growth rate γ depends on the integral of the perpendicular gradient of the electron distribution f along the resonance condition (1):$\gamma \propto \int_{R.C.} v_{\perp}^2 \nabla v_{\perp} f(v)\, dv$.

[10] The growth rate is positive (amplification) if the integral of the gradient $\nabla v_{\perp} f(v)$ is positive. The beaming angle function $\theta(f)$ in equation (2) depends on the resonance circle along which the integral is largest, and thus on the shape of the electron distribution involved in the radio wave generation. Two distributions unstable relative to the CMI and commonly observed in the (Earth's) auroral regions, are the loss-cone generated by the magnetic mirroring and collisional loss of precipitating particles in the Jovian ionosphere, and the horseshoe/shell generated by parallel acceleration in the flux tube followed by adiabatic particle propagation in a converging magnetic field geometry [*Ergun et al.*, 2000]. These distributions are sketched on Figure 1. The regions of the plane where $\nabla v_{\perp} f(v) > 0$ are emphasized by red arrows. The resonance circles leading to maximum amplification are displayed, and their center $v_{||o}$ is, for a loss-cone distribution:

$$v_{\|o} = v/\cos\alpha = v/\left(1 - \omega_{ce}/\omega_{ce,max}\right)^{1/2} \quad (3)$$

where $\alpha = \arcsin((\omega_{ce}/\omega_{ce,max})^{1/2})$ is the loss-cone angle (represented on Figure 2a), and $\omega_{ce,max}$ the maximum electron cyclotron frequency at the active field line footprint. The radio beaming angle is then obtained from equation (2), as:

$$\theta = \arccos\left[(v/c)/\left(1 - \omega_{ce}/\omega_{ce,max}\right)^{1/2}\right] \quad (4)$$

It is plotted on Figure 2b for three values of the resonant particle velocity corresponding to electrons energies of 0.64, 2.5 and 10 keV. The beaming angle starts from a nearly-asymptotic maximum value between 78° and 87° at low frequencies and decreases steeply when the frequency gets close to the maximum frequency (at field line footpoint). It increases with electron energy.

[11] For a shell distribution Figure 1 shows that, as $\nabla v_{\perp f}(v) > 0$ just inside the shell, one has $v_{||o} = 0$ and thus $\theta = 90°$ whatever the frequency or resonant particle velocity. However refraction effects on the shell instability are expected to be non-negligible, even in the strongly magnetized Jovian auroral regions. The existence of a solution of equation (1) for $k_{||} v_{||} = 0$ implies that the emission frequency is lower than the cyclotron frequency: $\omega = \omega_{ce}/\Gamma \sim \omega = \omega_{ce}(1 - v^2/(2c^2))$. Thus the source must lie in an auroral cavity (cold plasma depleted region) where the radiation can propagate below the electron gyrofrequency [*Pritchett et al.*, 2002]. The waves are then strongly refracted at the borders of the cavity. In the Earth's auroral regions ($\omega_{ce} \geq \omega_{pe}$) this refraction leads to beaming angles as low as 40°, but at Jupiter ($\omega_{ce} \gg \omega_{pe}$) it is expected to lead to larger values such as 75°–80° (R. L. Mutel, personal communication, 2008). It must also be noted that the loss-cone (or "oblique") instability is effective not only in the case of a loss-cone distribution, but also applied to other auroral distributions (horseshoe, ring), while the shell instability describes the perpendicular emission from all these distributions [*Hess et al.*, 2008].

3. Simulation

[12] Our aim is to simulate a few representative Io-Jupiter arc shapes in the t-f plane by computing the geometrical visibility of radio sources located along an active field line. We selected for that purpose the typical arcs displayed in Figure 1 of QZ98, reproduced here in Figures 3a–3c and listed in Table 1. These arcs were observed simultaneously by the Wind spacecraft (Waves experiment, <14 MHz) and the Nançay decameter array (>14 MHz), providing full coverage of their frequency range from 1 to 40 MHz. Figure 3a reveals an Io–B arc from the northern hemisphere and an Io–D arc from the southern hemisphere (as confirmed by their polarization and morphology). Figure 3b shows an Io–C (southern) arc, and Figure 3c several Io–A (northern) and possibly weak Io–C emission.

[13] We developed a general simulation code named "PRES" (Planetary Radio Emission Simulator) which computes the visibility of planetary radio sources from a given observer. In our case, radio sources are located along a field line leading the instantaneous IFT by an angle δ (and thus rotating with Io), and radio emission is assumed to be generated by the CMI at the local f_{ce}. The magnetic field is computed using the VIT4, fourth order model of the Jovian internal field (J. E. P. Connerney, personal communication, 2007). This model is derived from IR observations of the IFT footprints scaled by Voyager's magnetometer measurements. It is believed to be the most accurate field model for field lines crossing Io's orbit. The code computes at all frequencies and times of interest (i) the angle between the direction of the magnetic field in the source (in both hemispheres) and the observer's line of sight, and (ii) the radio beaming angle predicted by the loss-cone driven (oblique, equation (4)) or shell driven (perpendicular) CMI. When these two angles differ by less than the assumed cone thickness (actually by less than $\pm\theta/2$), we conclude that radio emission is received at the corresponding time and frequency. Note that the topology of the emitting field line varies with its longitude $\Lambda = \Lambda_{Io} - \delta$, thus with the time. The simulated dynamic spectrum displays information about the morphology of the emission in the t-f plane and on its hemisphere of origin, but no information on its

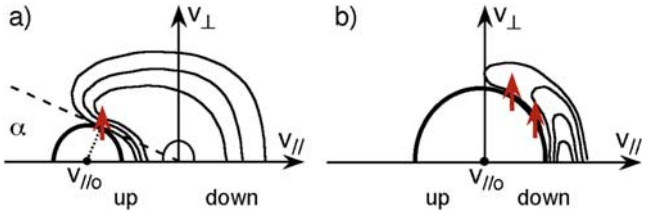

Figure 1. (a) Sketch of a loss-cone distribution. The loss-cone is the depleted domain of pitch angle $\alpha = \arctan(v_{||}/v_{\perp})$ in upgoing electrons. The largest positive gradient $\nabla v_{\perp}$ of the distribution function (red arrow) is on the border of the cone, at some resonant velocity v. The CMI resonance circle leading to maximum amplification is tangent to it and centered on $v_{||o} = v/\cos\alpha$. (b) Sketch of a shell distribution. The positive gradients $\nabla v_{\perp}$ of the distribution function are along the inner border of the shell. The CMI resonance circle leading to maximum amplification is tangent to it and centered on $v_{||o} = 0$.

intensity or on the conditions at the source that actually allow CMI to operate (thus, some predicted emissions may be absent of observed data if they originate from radio-sources where CMI is inefficient or if they are weaker than the detection threshold of the observations).

4. Results

[14] For simulating QZ98 arcs, we use the actual ephemeris of Io (Λ_{Io}, L-shell) and of the observer (Λ, distance), corresponding to the times of observation. Free parameters are the lead angle δ, the type of instability (oblique, perpendicular) and the energy or velocity (v) of resonant electrons, and the corresponding radio beaming ($\theta(f)$ and $\delta\theta$). Temporal and spectral resolutions of the simulated dynamic spectra are here 0.5 minute (over the whole duration of the observations) $\times$50 kHz (from 1 to 40 MHz). The aim of this first study is a qualitative fit of arc shapes providing constraints on the above parameters, not a detailed fit by exhaustive exploration of the parameter space, that will be the purpose of a further study.

[15] Figure 3d displays a dynamic spectrum of Io–B and Io–D arcs simulated with $\delta \sim 7°$, loss-cone driven CMI with electrons' energy of 0.6 to 3 keV (thus $\theta \rightarrow 84°–87°$ at low frequencies), and cone thickness $\delta\theta = 0.5°$ to $1°$ (see Table 1). Although there is a ~20 min. shift with the observed arcs of Figure 3a, and the simulated Io–B arc reaches frequencies lower than the observed one, the overall shape of simulated arcs, which represent all the Io-induced radio emission detectable in the displayed t-f interval, is remarkably similar to that of the observed ones.

[16] In Figure 3e, the Io–C arc simulated with the same parameters as the Io–D arc above (see Table 1) also matches well the observed one (of Figure 3b), except for its early part before ~23:00. A northern Io–A arc is also necessarily predicted (here displayed with δ arbitrarily set to 20°), but not observed in Figure 3b. This may be due to an intrinsic time variability of Io-induced radio emission, or to the fact that although the visibility condition would allow to detect this arc, the conditions for its generation by the CMI are not verified near the northern IFT footprint for this geometry of observation.

[17] Figure 3f attempts to account for the observation (in Figure 3c) of several Io–A arcs between ~20:00 and 22:00, as well as possibly a weak Io–C one at ~22:30. The Io–A arcs are reasonably well simulated using the same parameters as for the Io–B arc above, except that they require multiple lead angles of 20°, 30° and 40° (possibly due to Alfvén wave reflexions). The Io–C arcs are obtained for δ = 15° and 20°, with the first value corresponding to the later Io–C arc, consistent with the weak one observed. The non-detection of the nearly horizontal part of Io–C arcs in Figure 3c may be due to the interference between ~14 and 20 MHz, or to the fact that the corresponding emission is generated just above the ionosphere and thus possibly weakly amplified (the loss-cone is widely open, thus the gradient in $f(v)$ is rather in the direction of $v_{||}$). Figures 3g–3i show the simulation results for the same parameters as resp. Figures 3d–3f, except that $\theta(f)$ is taken constant and equal to 82°. This represents shell-driven CMI, where the value of θ is chosen smaller that 90° to include near-source refraction effects, as discussed in section 2. The resulting arcs poorly fit the observed ones, in consistency with the results of *Lecacheux et al.* [1998]. The good quality of the fit between simulations 3def and observations 3abc, and the large difference with 3ghi in the arc morphology at high frequency, is thus entirely due to the decrease of the radio

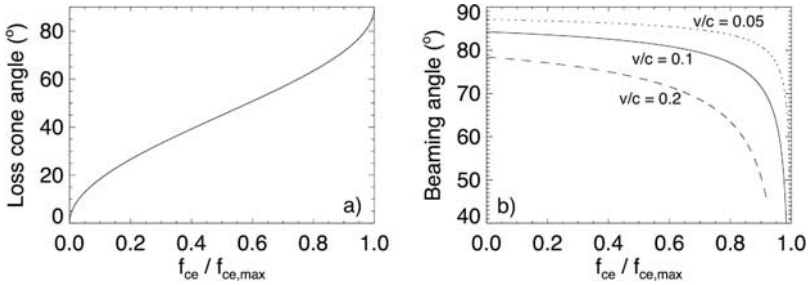

Figure 2. (a) Loss-cone angle versus cyclotron frequency along a magnetic field line [$\alpha = \arcsin((f_{ce}/f_{ce,max})^{1/2}$]. Along the IFT, $f_{ce} \sim 60$ kHz at the equator, so that the loss-cone angle at the equator is $\alpha = 2.56°, 2.37°, 2.22°$ for $f_{ce,max}$ = 30, 35, 40 MHz at IFT footprints. (b) Radio beaming angle versus normalized cyclotron frequency $f_{ce}/f_{ce,max}$, for three values of the resonant electron velocity v corresponding to energies of 0.64, 2.5 and 10 keV, in the case of an emission due to an oblique (loss-cone) instability.

beaming angle at high frequency, as previously deduced by *Goldstein and Thieman* [1981] and QZ98.

5. Discussion

[18] Simulation of a few representative Io-induced radio arcs and qualitative comparison to observed ones clearly demonstrates that: (i) all observed arc shapes can be correctly modelled only in the frame of oblique CMI (even if the energy source in the electrons distribution is not a loss-cone but, e.g., a ring of particles), implying emission at large angle ($\geq 80°$) from the source magnetic field, except at high frequencies where $\theta(f)$ strongly decreases; (ii) the lead angle of the radio emitting field line is between a few degrees and $\sim 40°$, consistent with QZ98, but only partly consistent with the lead angle deduced from UV and IR measurements ($\leq 15°-20°$) [*Prangé et al.*, 1996; *Clarke et al.*, 2002]; (iii) the resonant electron energy is about a few keV, consistent with previous determinations [and references therein *Hess et al.*, 2007]. The electron energy appears higher in the southern than in the northern hemisphere, leading to larger radio beaming angles in the north (as noticed by QZ98). This may be due to the fact that Io is located to the north of the torus center in the domain of Λ_{Io} where emission occurs, leading to an asymmetric Io-Jupiter interaction; (iv) the cone thickness (which controls the arc thickness in the t-f plane) is of the order of 0.5° to 1°, consistent with QZ98 and *Kaiser et al.* [2000].

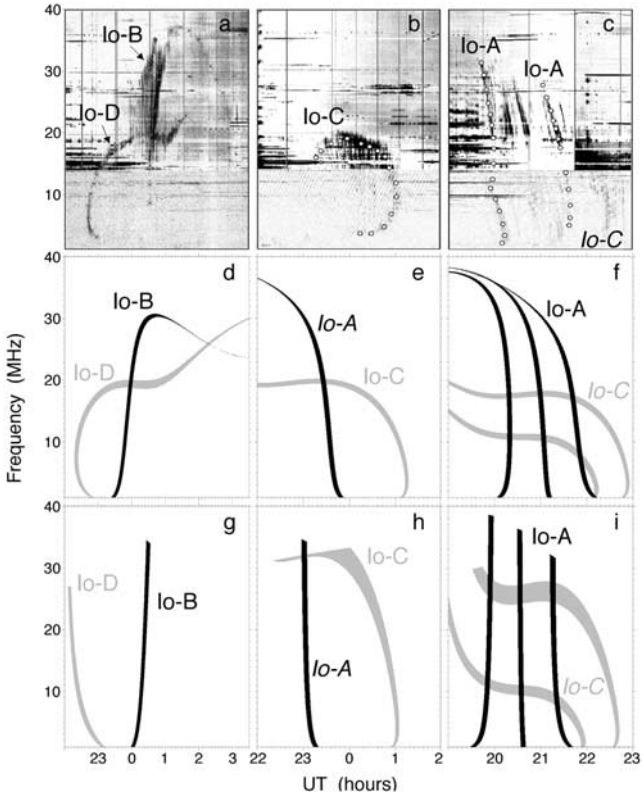

Figure 3. (a, b, c) Dynamic spectra of typical Io-Jupiter arcs observed by Wind/Waves and the Nançay decameter array, studied by QZ98, and listed in Table 1 (adapted from Figure 1 of QZ98; the various symbols superimposed along the arcs were used to identify their line of maximum intensity in the t-f plane). (d, e, f) Dynamic spectra of Io-Jupiter emission for the same t-f intervals as in Figures 3a, 3b, and 3c, simulated by the PRES code using actual observing geometries (defined by Λ_{Io}, Io L-shell, $\Lambda_{observer}$, and observer-source distance), and the parameters listed in Table 1. Black arcs are generated in the northern hemisphere and grey in the southern one. Labels in italics indicate weak or unobserved arcs. (g, h, i) Same as Figures 3d, 3e, and 3f except that $\theta(f)$ is taken constant and equal to 82°.

Table 1. Parameters of Simulated Io-Jupiter Arcs of Figure 3

Date of Observation	Arc Type (Hemisphere)	Lead Angle δ	Resonant Electrons Velocity v (Energy)	$\delta\theta$	Figure
8–9/5/1995	Io–B (N)	6°	0.05c (0.64 keV)	1°	Figure 3d
8–9/5/1995	Io–D (S)	8°	0.11c (3 keV)	0.5°	Figure 3d
7–8/5/1995	Io–C (S)	8°	0.11c (3 keV)	0.5°	Figure 3e
7–8/5/1995	Io–A (N)	20°	0.05c (0.64 keV)	1°	Figure 3e
22/9/1997	Io–A (N)	20°, 30°	0.05c (0.64 keV)	1°	Figure 3f
22/9/1997	Io–C (S)	15°, 20°	0.11c (3 keV)	0.5°	Figure 3f

[19] At Earth, radio emission occurs in auroral cavities where both oblique and perpendicular CMI can occur. In that case, the latter dominates due to higher growth rates [*Louarn*, 1992]. At Jupiter, *Hess et al.* [2008] have shown that because oblique CMI can occur out of any high-latitude cavity, it may dominate the Jovian radio spectrum. The above results suggest that Io-induced arcs are indeed generated outside plasma cavities. Absence of formation of cavities at the IFT footprints could be due to the brief excitation of a Jovian field line by the passage of Io ($\sim$1 min.).

[20] No combination of δ and θ allowed us to simulate an Io–B arc reaching frequencies as high as in Figure 3a. A modification of the Jovian magnetic field model is required for that (which could also improve the temporal correspondence of simulated and observed arcs). It should also be noted that the observed arc shapes are not well reproduced at low frequencies (<5 MHz). This may be improved by taking into account refraction effects as the source gets closer to the Io plasma torus border (where ω_{ce}/ω_{pe} decreases, and $N \neq 1$ in equation (2)), as done by L. C. Ray and S. Hess (Modelling the Io-related DAM emissions by modifying the beaming angle, submitted to *Journal of Geophysical Research*, 2008).

[21] The next step will be an extensive parametric fit of many Io-induced arcs observed by ground-based radiotelescopes (Nançay, Kharkov), Voyager and Cassini spacecraft for various observing geometries, in order to derive δ, $\theta(f)$, $\delta\theta$, and v as a function of Λ_{Io}, $\Lambda_{observer}$, time, and latitude of the observer (the latter was assumed to be 0° in the present study, but it can actually take values within ±3.3°). Full modeling should include computation of the wave amplification as in the work by *Hess et al.* [2008].

[22] **Acknowledgments.** We thank J. E. P. Connerney for providing us with the VIT4 magnetic model and R. L. Mutel for his valuable comments.

References

Carr, T. D., M. D. Desch, and J. K. Alexander (1983), Phenomenology of the magnetospheric radio emissions, in *Physics of the Jovian Magnetosphere*, *Cambridge Planet. Sci. Ser.*, vol. 3, edited by A. J. Dessler, pp. 226–284, Cambridge Univ. Press, New York.

Clarke, J. T., et al. (2002), Ultraviolet auroral emissions from the magnetic footprints of Io, Ganymede, and Europa on Jupiter, *Nature*, *415*, 997–1000.

Ergun, R. E., C. W. Carlson, J. P. McFadden, G. T. Delory, R. J. Strangeway, and P. L. Pritchett (2000), Electron-cyclotron maser driven by charged-particle acceleration from magnetic field-aligned electric fields, *Astrophys. J.*, *538*, 456–466.

Goldstein, M. L., and J. R. Thieman (1981), The formation of arcs in the dynamic spectra of Jovian decameter bursts, *J. Geophys. Res.*, *86*, 8569–8578.

Hess, S., P. Zarka, and F. Mottez (2007), Io-Jupiter interaction, millisecond bursts and field aligned potentials, *Planet. Space Sci.*, *55*, 89–99.

Hess, S., F. Mottez, P. Zarka, and T. Chust (2008), Generation of the Jovian radio decametric arcs from the Io flux tube, *J. Geophys. Res.*, *113*, A03209, doi:10.1029/2007JA012745.

Kaiser, M. L., P. Zarka, W. S. Kurth, G. B. Hospodarsky, and D. A. Gurnett (2000), Cassini and Wind stereoscopic observations of Jovian nonthermal radio emissions: Measurement of beam widths, *J. Geophys. Res.*, *105*, 16,053–16,062.

Lecacheux, A., M. Y. Boudjada, H. O. Rucker, J. L. Bougeret, R. Manning, and M. L. Kaiser (1998), Jovian decameter emissions observed by the Wind/WAVES radioastronomy experiment, *Astron. Astrophys.*, *329*, 776–784.

Louarn, P. (1992), Auroral planetary radio emissions: Theoretical aspects, *Adv. Space. Res.*, *12*(8), 121–134, doi:10.1016/0273-1177(92)90385-B.

Neubauer, F. M. (1980), Nonlinear standing Alfven wave current system at Io: Theory, *J. Geophys. Res.*, *85*, 1171–1178.

Prangé, R., D. Rego, D. J. Southwood, P. Zarka, S. Miller, and W.-H. Ip (1996), Rapid energy dissipation and variability of the Io-Jupiter electrodynamic circuit, *Nature*, *379*, 323–325.

Pritchett, P. L., R. J. Strangeway, R. E. Ergun, and C. W. Carlson (2002), Generation and propagation of cyclotron maser emissions in the finite auroral kilometric radiation source cavity, *J. Geophys. Res.*, *107*(A12), 1437, doi:10.1029/2002JA009403.

Queinnec, J., and P. Zarka (1998), Io-controlled decameter arcs and Io-Jupiter interaction, *J. Geophys. Res.*, *103*, 26,649–26,666.

Saur, J., F. M. Neubauer, J. E. P. Connerney, P. Zarka, and M. G. Kivelson (2004), Plasma interaction of Io with its plasma torus, in *Jupiter: The Planet, Satellites, and Magnetosphere*, *Cambridge Planet. Sci. Ser.*, vol. 1, edited by F. Bagenal, T. E. Dowling, and W. B. McKinnon, pp. 537–560, Cambridge Univ. Press, Cambridge, U.K.

Wu, C.-W. (1985), Kinetic cyclotron and synchroton maser instabilities: Radio emission processes by direct amplification of radiation, *Space Sci. Rev.*, *41*, 215–298.

B. Cecconi, S. Hess, and P. Zarka, LESIA, Observatoire de Paris, UPMC, CNRS, 5 Place Jules Janssen, F-92190 Meudon, France. (sebastien.hess@obspm.fr)